



RESEARCH ARTICLE

10.1029/2023SW003689

A Comparison of Auroral Oval Proxies With the Boundaries of the Auroral Electrojets

Simon James Walker¹ , Karl Magnus Laundal¹ , Jone Peter Reistad¹ , Anders Ohma¹ ,
Spencer Mark Hatch¹ , Gareth Chisham² , and Margot Decotte¹ 

¹Department of Physics and Technology, University of Bergen, Bergen, Norway, ²British Antarctic Survey, Cambridge, UK

Key Points:

- We present a new electrojet boundary data set and compare it with auroral oval proxies
- On average proton aurora boundaries are more aligned with electrojet boundaries than electron aurora boundaries
- Noon and midnight electrojet discontinuities present a problem for auroral oval determination from electrojet boundaries

Correspondence to:

S. J. Walker,
simon.walker@uib.no

Citation:

Walker, S. J., Laundal, K. M., Reistad, J. P., Ohma, A., Hatch, S. M., Chisham, G., & Decotte, M. (2024). A comparison of auroral oval proxies with the boundaries of the auroral electrojets. *Space Weather*, 22, e2023SW003689. <https://doi.org/10.1029/2023SW003689>

Received 28 AUG 2023

Accepted 14 MAR 2024

Author Contributions:

Conceptualization: Simon James Walker, Karl Magnus Laundal, Jone Peter Reistad, Anders Ohma, Spencer Mark Hatch, Gareth Chisham

Data curation: Simon James Walker

Formal analysis: Simon James Walker

Funding acquisition: Karl Magnus Laundal

Investigation: Simon James Walker

Methodology: Simon James Walker

Resources: Gareth Chisham, Margot Decotte

Supervision: Karl Magnus Laundal, Jone Peter Reistad, Anders Ohma, Spencer Mark Hatch

Visualization: Simon James Walker

Writing – original draft: Simon James Walker

Writing – review & editing: Simon James Walker, Karl Magnus Laundal, Jone Peter Reistad, Spencer Mark Hatch, Gareth Chisham, Margot Decotte

Abstract The boundaries of the auroral oval and auroral electrojets are an important source of information for understanding the coupling between the solar wind and the near-earth plasma environment. Of these two types of boundaries the auroral electrojet boundaries have received comparatively little attention, and even less attention has been given to the connection between the two. Here we introduce a technique for estimating the electrojet boundaries, and other properties such as total current and peak current, from 1-D latitudinal profiles of the eastward component of equivalent current sheet density. We apply this technique to a preexisting database of such currents along the 105° magnetic meridian, estimated using ground-based magnetometers, producing a total of 11 years of 1-min resolution electrojet boundaries during the period 2000–2020. Using statistics and conjunction events we compare our electrojet boundary data set with an existing electrojet boundary data set, based on *Swarm* satellite measurements, and auroral oval proxies based on particle precipitation and field-aligned currents. This allows us to validate our data set and investigate the feasibility of an auroral oval proxy based on electrojet boundaries. Through this investigation we find the proton precipitation auroral oval is a closer match with the electrojet boundaries. However, the bimodal nature of the electrojet boundaries as we approach the noon and midnight discontinuities makes an average electrojet oval poorly defined. With this and the direct comparisons differing from the statistics, defining the proton auroral oval from electrojet boundaries across all local and universal times is challenging.

Plain Language Summary The global location of the northern and southern lights (aurora) holds particular importance for understanding where energy from the solar wind and its coupling with the magnetosphere is deposited in the upper atmosphere. The brightness of these lights and related electrical currents also indirectly indicate the magnitude of the energy deposition. However, global imaging of aurora is limited by sunlight, with generally fewer observations during summer months. Furthermore, global observations are not possible from the ground, and space-based global imaging has been missing for close to two decades. In this study we investigate alternative methods, with particular emphasis on a technique exploiting ground magnetometer data. Electrical currents have been robustly mapped for two decades over Fennoscandia, without observational limitations due to season. We investigate how the average location of these currents relates to the average location of the aurora and other related current systems. We use these results to discuss the feasibility of finding the location of the aurora from a more abundant data source and increasing the understanding of the underlying mechanisms.

1. Introduction

The boundaries of the auroral oval are natural points of reference for understanding and organizing polar ionospheric electrodynamics (Andersson et al., 2004; Burrell et al., 2020; Kilcommons et al., 2017; Redmon et al., 2010). The poleward boundary of the auroral oval is a commonly used proxy of the boundary between open and closed magnetic field lines (OCB) and, therefore, can be used to determine the amount of open magnetic flux contained within the polar cap and is commonly used to describe the magnetic energy stored in the magnetotail (Milan et al., 2007, 2017). The equatorward boundary describes the extent of where this additional energy translates into enhanced auroral activity (precipitation, strengthened auroral electrojets etc.) and is important in understanding where space weather hazards are heightened (Carbary, 2005). The auroral electrojets are often described as flowing within the auroral oval (Johnsen, 2013) and measurements of the electrojets are often reduced to singular metrics to describe the state of polar ionospheric activity (i.e., Auroral Lower index, Auroral Upper index, etc.) (Kamide & Akasofu, 1983; Rostoker et al., 1980).

© 2024. The Authors.

This is an open access article under the terms of the [Creative Commons Attribution License](https://creativecommons.org/licenses/by/4.0/), which permits use, distribution and reproduction in any medium, provided the original work is properly cited.

The auroral oval is typically phenomenologically defined by auroral emissions or through the populations of energetic particle precipitation (Chisham et al., 2022; Decotte et al., 2023; Feldstein & Starkov, 1967; Holzworth & Meng, 1975; Kilcommons et al., 2017; Longden et al., 2010; Zou et al., 2012). Thresholds of the total precipitating electron energy flux are an often used proxy of the OCB (Boakes et al., 2008; Longden et al., 2010). However, ground-based auroral observations, which began prior to the advent of space-based observations, are limited by location and condition requirements, such as clouds, lunar illumination and solar illumination. A number of satellite auroral observations are able to image the entire auroral oval and therefore can provide global boundaries, however they are limited by the time when the satellite was in operation, satellite orbit and to some extent solar illumination because of dayglow (Ohma et al., 2023). Particle detectors onboard satellites, such as the Defense Meteorological Space Program (DMSP) satellites, have enabled routine determination of auroral oval boundaries through identification of auroral particle precipitation populations (Kilcommons et al., 2017). An advantage of these measurements is they are not restricted by dayglow and solar illumination but they are limited to point observations along the satellite path. Decotte et al. (2023) have also shown that auroral boundaries identified via DMSP Special Sensor J (SSJ) electrostatic analyzers are biased in some local time sectors due to the trajectory of these satellites through the auroral zone.

Both field-aligned currents (FACs) and the auroral electrojets can be estimated from their magnetic field signatures using magnetometers onboard satellites such as CHALLENGING Minisatellite Payload (CHAMP) and the *Swarm* satellites and have been compared with the auroral oval (Feldstein et al., 1999; Xiong & Lühr, 2014). Routines have been designed to find the FAC boundaries and electrojet boundaries, with advantages and disadvantages similar to those of boundary estimates made using satellite-based particle instruments (Aakjær et al., 2016; Juusola et al., 2006; Kervalishvili et al., 2020; Viljanen et al., 2020; Xiong & Lühr, 2014; Xiong et al., 2014). Historically, however, estimates of the electrojets have predominantly been made using ground based magnetometers (Harang, 1946). Like satellite magnetometers, ground-based magnetometers are not challenged by weather and solar illumination but additionally have the advantage of being fixed geographically (i.e., can remain in and around the auroral zone and ionospheric interaction region). Such measurements have generally been made at 1-min cadence for the last few decades, and more recently 10-s and even 1-s cadence. However, accurate background magnetic field estimates are required for baseline removal in order to retrieve the real magnitude of perturbations. Additionally, ground magnetometers are limited by location and operation, where more inaccessible sites generally experience more down time and areas of sea or completely inaccessible areas of land produce gaps in the distribution of magnetometers. Furthermore, ground induced currents can obscure the derivation of the ionospheric current particularly when it is assumed the magnetic field perturbations are purely of ionospheric origin.

The clear advantages of ground based magnetometers, in terms of data coverage and reliability, make it important to use the measurements to identify the boundaries of the auroral electrojets and understand their place in describing the auroral oval. Thus enhancing our knowledge of the auroral oval when more typical measurements are lacking and gaining a greater understanding of the links between ionospheric processes. To our knowledge, three studies have used an algorithm based approach to identify the boundaries of the auroral electrojets on the basis of ground magnetometer measurements (Feldstein et al., 1999; Johnsen, 2013; Kisabeth & Rostoker, 1971). In all of these studies the radial component of magnetic field perturbations was primarily used for determination of the latitudinal extent of the auroral electrojets, and in only one of these was a limited comparison with auroral oval boundaries carried out (Feldstein et al., 1999). Kisabeth and Rostoker (1971) used a set of magnetometers around the 302° magnetic meridian (Western Canada), and defined the boundaries of the auroral electrojet as the location of the maxima and minima in the radial component that flank the zero point of the radial component or the peak in the horizontal component. They investigated how the width and peak varied during a selection of substorms. Johnsen (2013) modeled the auroral electrojet as a set of line currents, with amplitudes obtained from fits to the ground magnetic field measured by ground magnetometers in Scandinavia. They then estimated the electrojet boundaries algorithmically using the same criteria described by Kisabeth and Rostoker (1971). These boundaries are then provided to real time tracking and alerts for auroral activity, such as the Advanced Forecast For Ensuring Communications Through Space project (Bothmer et al., 2013).

In Section 2 we estimate the electrojet boundaries from minute resolution electrojet current profiles along the 105° magnetic meridian presented by S. Walker, Laundal, Reistad, Hatch, et al. (2023) (S. J. Walker et al., 2022), which yields a database spanning a total of 11 years during the 21-year period between 2000 and 2020 (S. J. Walker, Laundal, Reistad, Hatch, et al., 2023). In Section 3 we compare these boundaries both in case studies and

Table 1

The Data Sets Used in This Study, the Type of Boundaries They Identify, the Measurements Used to Derive Them and the Time Span of the Data That Is Used in This Study

Boundary data set	Boundary type	Measurements	Time span
Current Paper (GBM) (S. J. Walker, Laundal, Reistad, Hatch, et al., 2023)	Auroral Electrojets	Ground Based Magnetometers (S. J. Walker et al., 2022) (S. Walker, Laundal, Reistad, Hatch, et al., 2023)	2000–2020
Swarm (SBM) (Viljanen et al., 2020)	Auroral Electrojets	Swarm Magnetometers (Kervalishvili et al., 2020)	2013–2023
SI12 (Chisham et al., 2022)	Aurora	Space Based Imager (IMAGE)	2000–2003
SI13 (Chisham et al., 2022)	Aurora	Space Based Imager (IMAGE)	2000–2003
DMSP (Kilcommons et al., 2017)	Precipitation	Space Based Particle Detector	2001–2016
CHAMP Model (Xiong & Lühr, 2014)	Field Aligned Currents	CHAMP Magnetometer (Xiong et al., 2014)	2000–2010 ^a

^aFor this case this is the range of data used to create the boundaries in Xiong et al. (2014) that are used to create the model in Xiong and Lühr (2014).

statistically with auroral electrojet boundaries estimated via satellite-borne magnetometers, auroral oval boundaries found using particle precipitation measurements from DMSP satellites (Decotte et al., 2023; Kilcommons et al., 2017), a merging electric field scaled model of the FAC boundaries (Xiong & Lühr, 2014; Xiong et al., 2014) and auroral oval boundaries found using satellite based far ultra violet (FUV) measurements of the aurora (Chisham et al., 2022; Longden et al., 2010). In Section 4 we discuss these comparisons and how the auroral electrojet boundaries relate to the auroral oval both on average and on a case by case basis.

2. Data and Methodology

In this section we describe the different boundary data sets used in this study and the methodology behind them. Table 1 summarizes these data sets. We also describe the parameters we use to bin our data.

2.1. Electrojet Boundaries From Regionally Constrained Divergence Free Currents

We now describe how we derive the database of electrojet boundaries and properties based on the minute-resolution sheet current density profiles produced by S. Walker, Laundal, Reistad, Hatch, et al. (2023).

2.1.1. Estimating the Electrojet Currents

The core component of S. Walker, Laundal, Reistad, Hatch, et al. (2023) and how they estimate the divergence-free ionospheric currents is the spherical elementary current systems (SECS) method. The superposition of an appropriately scaled collection of SECS basis functions can recreate any two-dimensional current system that exists on a spherical shell, such as the divergence-free ionospheric currents (Amm, 1997; Amm & Viljanen, 1999; Vanhamäki & Juusola, 2020). Amm (1997) introduced divergence-free SECS basis functions with this purpose in mind, and described the current associated with each type of basis function. Amm and Viljanen (1999) then derived analytic expressions for the corresponding magnetic field. These expressions for the magnetic field enable estimation of the amplitude of each member of a collection of SECS basis functions from measurements of the magnetic field via a linear inverse problem. Once these amplitudes are known, it is straightforward to calculate the total divergence-free current system that can represent the measured magnetic field. S. Walker, Laundal, Reistad, Hatch, et al. (2023) used measurements made by a fixed set of 20 ground magnetometers in Fennoscandia to constrain their SECS model along with regularization of the east–west gradient and the amplitude of the model vector. Using this model, the divergence-free ionospheric sheet current density was estimated along the 105° magnetic meridian for each minute when the magnetometers were available concurrently over the 20 year period from 2000 to 2020 (S. J. Walker et al., 2022). Using the same magnetometers throughout the data set and only estimating currents when all 20 are available produces gaps within the data set, reducing the size of the data set to the equivalent of 11 years. Furthermore, the data set is poorly constrained at high latitudes (we return to how this affects our electrojet boundaries in the next subsection) and does not extend beyond 81° MLat. The strict approach to the magnetometers in S. Walker, Laundal, Reistad, Hatch, et al. (2023) appears limiting but it is essential for the validity of the statistics in the study and it is essential for the work conducted within this study, which we describe further in the next subsection. When changing the selection of magnetometers the estimated currents will change without any change to the true current. This can invalidate statistical studies or comparisons between different

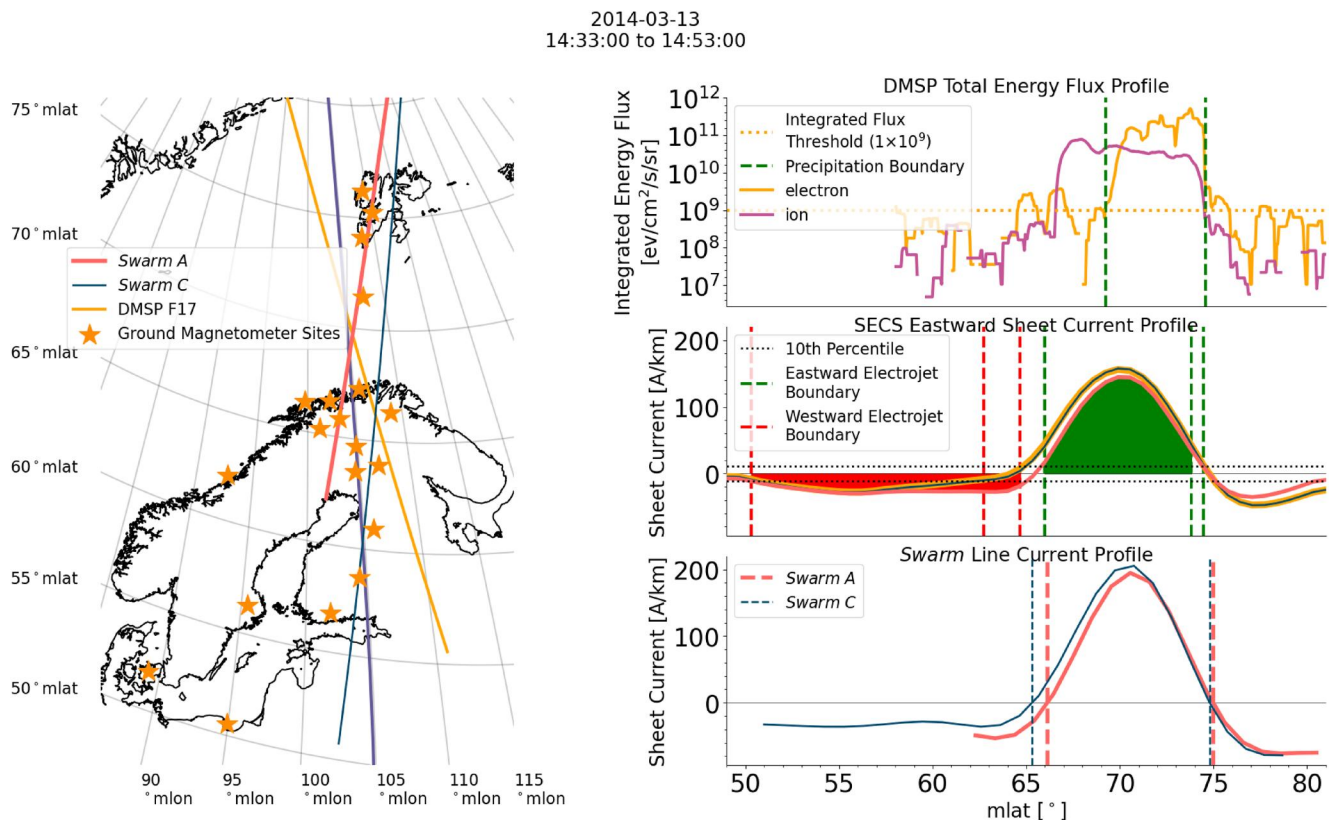


Figure 1. Conjunction event between the 105° magnetic meridian, *Swarm A*, *Swarm C* and Defense Meteorological Space Program (DMSP) F17. The 105° magnetic meridian goes from approximately 16.5 to 16.9 MLT and $\bar{\epsilon}_N$ ranges from 3.6 to 4.3. The left panel shows a map of Fennoscandia and the location of the 20 magnetometers used by S. Walker, Laundal, Reistad, Hatch, et al. (2023), the satellite trajectories and the 105° magnetic meridian. Magnetic latitudes and longitudes are given in Apex coordinates. Top right panel: DMSP F17 proton and electron energy flux measurements integrated for particles with energy between 1.3 and 30 keV. Vertical green lines show the auroral oval boundaries found via the Kilcommons et al. (2017) method, and the dotted horizontal orange line shows the associated integrated flux threshold. Middle right panel: an application of the algorithm described in Section 2.1.2 to three median sheet current density profiles. Each median sheet current density profile is constructed by finding the median of the eastward sheet current density in S. J. Walker et al. (2022) between the time of the boundaries found using DMSP F17, *Swarm A* and *Swarm C*. The color of each median profile indicates which satellite boundary times are used for the window to determine the median profile, following the same color convention as the left panel. The strongest east and west current sections found using the median profile associated with *Swarm A* are highlighted with their corresponding color. Bottom right panel: the sheet current density profiles found using *Swarm A* and *C* and their associated electrojet boundaries (Kervalishvili et al., 2020; Viljanen et al., 2020).

times as we can no longer attribute changes in the estimated currents to a change in physical conditions (e.g., convection, dayside reconnection rate etc).

2.1.2. Electrojet Algorithm

We now describe the algorithm we use to estimate the boundaries and properties of the auroral electrojets. The algorithm uses the latitudinal profile of the eastward component of the divergence-free sheet current density estimated by S. Walker, Laundal, Reistad, Hatch, et al. (2023). The estimation of these currents is briefly described in the previous subsection and the data set is available at S. J. Walker et al. (2022). The middle right panels of Figures 1 and 2 show examples of how the electrojet boundaries are estimated via the algorithm we will describe. Figures 1 and 2 are two occurrences where DMSP and *Swarm* satellites are in close proximity to the 105° magnetic meridian. The current profiles shown in the middle right panels of the Figures are the median of the eastward sheet current density data from S. J. Walker et al. (2022) that occurs between the times of the boundaries detected by the satellites during the event. This leads to one profile per satellite involved in the event. Although the focus of this study is the electrojet boundaries, the algorithm we employ estimates the poleward and equatorward boundary, the value and location of the peak sheet current, and the width and total current of multiple current sections, and proceeds as follows.

2014-02-22
16:14:22 to 16:37:34

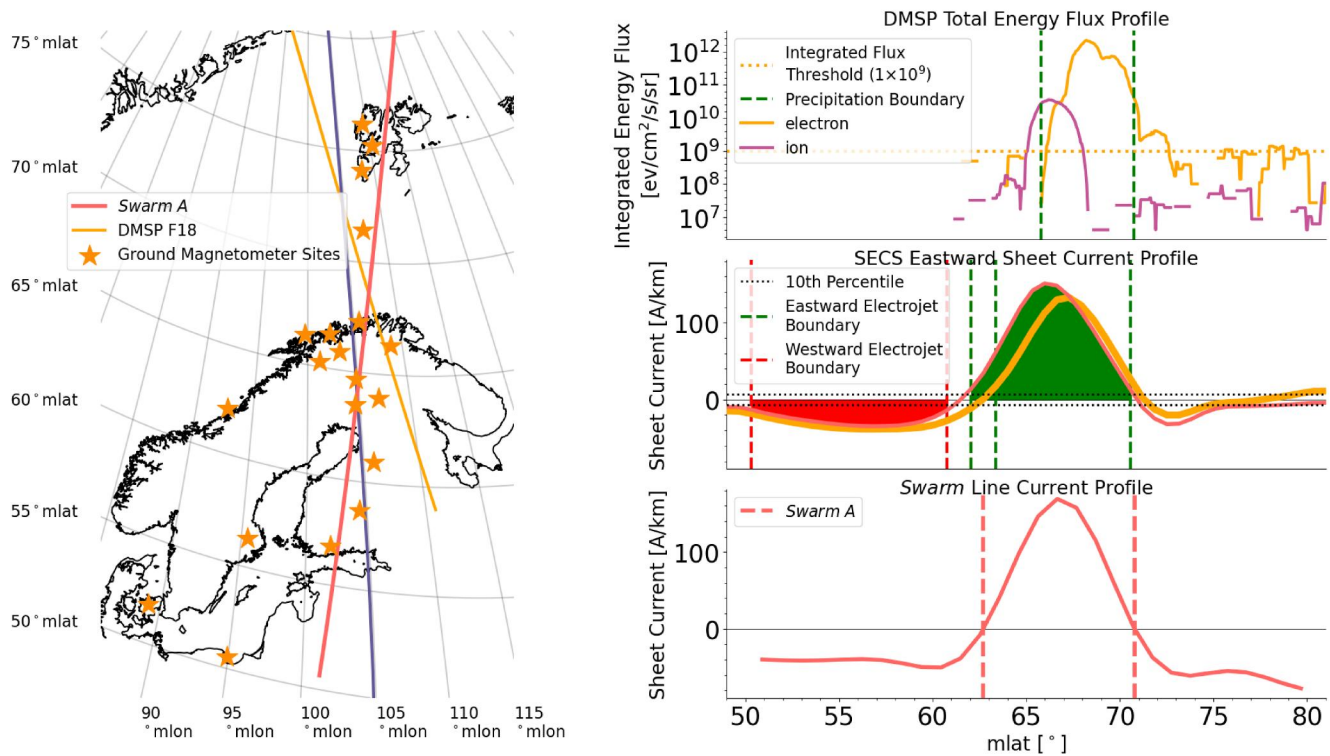


Figure 2. Conjunction event between the 105° magnetic meridian, *Swarm A* and Defense Meteorological Space Program F18, occurring between 16:14:22 and 16:37:34 UT on 22nd of February 2014, in the same format as Figure 1. The 105° magnetic meridian goes from approximately 18.2 to 18.6 MLT and $\bar{\epsilon}_N$ has a range of 5.4–6.1.

1. Initial boundary estimates are identified as the points where the current profile crosses positive or negative thresholds defined as the tenth percentile of the absolute current density or the latitude limits of the meridian (shown as thick black horizontal lines in the right middle panels of Figures 1 and 2 as thresholds for the red median profile). This procedure splits the current profile into different sections.
2. Since the current profiles quite often flatten just above the tenth percentile, in the next step the boundary is moved closer to where a clear peak is formed. This point is defined as the closest point to the peak where the gradient is still less than 60% of the mean absolute gradient in the electrojet section. The peak itself is excluded by ensuring that the current magnitude is less than 40% of the mean of the particular section. If a new boundary cannot be defined in this way, the initial estimate is kept. As such, the boundaries sometimes end up at or close to the low- and high-latitude edges of the meridian (respectively 49° and 81°). In such cases the full current section may not have been resolved and the boundaries should not be used.

The boundaries (shown as vertical dashed lines in Figures 1 and 2), peaks, widths, and total integrated current of the three strongest eastward and three strongest westward current sections are saved. In this study the strength is defined by the total integrated current of the profile (the strongest east and west current sections are highlighted in Figures 1 and 2, with their corresponding color, for the median profiles associated with the *Swarm A* satellite). This data set is publicly available: S. J. Walker, Laundal, Reistad, Hatch, et al. (2023). In this study we use the following criteria to deselect a number of boundaries deemed untrustworthy:

1. Boundaries occurring on first three (less than 50.5° MLat) and last three meridian data points (greater than 79.5°) are removed as the entire current section may not have been resolved
2. Eastward (westward) current sections must have peaks greater than 0.05 A.m.⁻¹ (less than -0.1 A.m.⁻¹) for their boundaries to remain. The thresholds are different because the westward electrojet is typically stronger than the eastward electrojet.

As we introduced in the previous subsection, the inclusion of additional magnetometers when estimating the current in S. Walker, Laundal, Reistad, Hatch, et al. (2023) may appear beneficial, particularly in regard to Equation 1. For example, the use of magnetometer data from the Station Nord would improve the latitudinal extent whenever the magnetometer data is available. However, this would lead to the possibility of electrojet boundaries at higher latitudes when we have measurements at Station Nord that would not be possible when we do not. Consequently, an increase in the latitude of the electrojet boundaries can no longer be solely attributed to physical changes. This can invalidate the use of statistics and temporal comparisons for investigating the physical conditions that control the location of the electrojet.

2.2. Swarm

We now outline the methodology of Aakjær et al. (2016), which is based on the work of Olsen (1996), for calculating sheet currents using *Swarm* magnetometers. This is the methodology used by Kervalishvili et al. (2020) to produce the publicly available sheet current data set. That can be obtained from <https://vires.services/> using the code SW_OPER_AEJALPL_2F, SW_OPER_AEJBLPL_2F, and SW_OPER_AEJCLPL_2F for *Swarm* A, B and C respectively. We also describe how Viljanen et al. (2020) and Kervalishvili et al. (2020) use these sheet current profiles to create a data set of Swarm-based electrojet boundaries (also available from <https://vires.services/> using the code SW_OPER_AEJAPBL_2F, SW_OPER_AEJBPBL_2F, SW_OPER_AEJCPBL_2F for *Swarm* A, B and C respectively).

Aakjær et al. (2016) represent the auroral electrojet as a series of line currents at an altitude of approximately 110 km separated by 113 km along and orientated perpendicular to the satellite track. Similar to the SECS approach, the amplitude of each line current is obtained as an inverse problem in which the superimposed magnetic field of the line currents is constrained by the magnitude of the magnetic field perturbations measured by the *Swarm* satellites, where the contribution from FACs is minimal. In Viljanen et al. (2020) these line currents are then transformed into the Quasi-Dipole magnetic east direction before applying the following electrojet algorithm:

1. Find the interpolated zero crossings of the current density curve.
2. Calculate the total current between crossings.
3. Define the electrojet as the series of current densities with the maximum total current or minimum in the case of the westward electrojet.

The data set is also provided with a set of quality flags that allow for the removal of spurious boundaries. In this study the quality flags were used to remove bad boundaries if any of the following conditions are true:

1. No eastward/westward currents detected.
2. The equatorward boundary occurs at the edge of the analysis area and the density is larger than 20% of peak value.
3. The poleward boundary occurs at the edge of the analysis area and the density is larger than 20% of peak value.
4. The *Swarm* orbit does not fully cover the predefined oval latitude range. The latitude gap is 2° or larger.
5. The equatorward boundary occurs at the edge of the analysis area.
6. The poleward boundary occurs at the edge of the analysis area.
7. The peak value occurs at the edge of the analysis area.

As both an eastward and westward electrojet can be detected in one oval crossing and only the peaks of the electrojets are provided, we choose the appropriate electrojet by the one with the largest peak magnitude.

2.3. Xiong FAC Boundaries

Xiong et al. (2014) use the magnetic field measurements made by CHAMP to estimate small- and medium-scale FACs. They then use these estimates to identify the boundaries of the FACs for each pass of the auroral oval. Xiong and Lüher (2014) bin these boundaries based on MLT and time integrated merging electric field (E_m), with the latter defined in terms of the Newell coupling function (ϵ_N). We return to define the ϵ_N in Section 2.6, where Equation 1 explains the function defined by Newell et al. (2007). For each E_m bin an ellipse is fit to the mean latitude of the poleward and equatorward boundaries across all MLT bins. Each ellipse parameter is represented by a quadratic in terms of E_m , with coefficients estimated using least squares, thus creating a model of the FAC boundaries that is dependent on ϵ_N .

2.4. Boundaries From Global Auroral Imagery

Longden et al. (2010) and Chisham et al. (2022) define an algorithm for identifying auroral boundaries in FUV images from the Imager for Magnetopause-to-Aurora Global Exploration (IMAGE) satellite (Mende, Heeterdks, Frey, Lampton, et al., 2000). They apply this algorithm to all three imagers on the IMAGE satellite, SI12, SI13 and WIC, creating three data sets. For this study we focus on the boundaries found using the SI12 and SI13 imagers (Mende, Heeterdks, Frey, Stock, et al., 2000), which measure emissions related to proton and electron precipitation respectively, as they have a reduced influence from dayglow compared to the WIC imager (Longden et al., 2010). The Chisham et al. (2022) auroral boundary algorithm proceeds as follows: (a) The locations of the pixels of the raw image are found in AACGM (Altitude Adjusted Corrected Geomagnetic) coordinates. (b) Measured intensities in the image are subdivided into bins of size 1 hr in MLT, the first bin being 0–1 MLT, and 1° MLat between 50° and 90° MLat. (c) A latitudinal intensity profile is constructed for each MLT segment. (d) This profile is then fitted by two different functions: the sum of a Gaussian function and a quadratic, and the sum of two Gaussian functions and a quadratic. The function with better goodness of fit is then chosen as the better fit. (e) In the case of a single Gaussian being the better fit the poleward and equatorward boundaries are determined by the peak of the Gaussian curve plus and minus the full width at half maximum (FWHM) of the Gaussian respectively. In the case of the double Gaussian the poleward boundary is determined by the peak of the Gaussian curve with the poleward maximum plus its FWHM and the equatorward boundary is determined by the peak of the Gaussian curve with the equatorward maximum minus its FWHM. Additional acceptance criteria for a successful boundary determination can be found in Longden et al. (2010) and Chisham et al. (2022).

2.5. DMSP (Kilcommons Algorithm)

The Kilcommons et al. (2017) algorithm estimates the auroral oval boundaries on the basis of precipitation measurements made by the SSJ instrument onboard DMSP satellites. Decotte et al. (2023) use a portion of this algorithm to produce auroral precipitation occurrence probability maps from the same measurements.

Using the total energy flux of electrons between 1.3 and 30 keV (J_E), Kilcommons et al. (2017) identify candidate auroral ovals as regions where J_E is greater than $10^9 \text{ eVcm}^{-2}\text{s}^{-1}\text{sr}^{-1}$ for polar passes that cross the auroral oval in two places. Using a figure of merit an auroral oval pair is selected from the candidates and the latitude limits recorded as auroral oval boundaries. Examples of these boundaries can be seen in the top right panel of Figures 1 and 2 along with the J_E latitude profile.

Decotte et al. (2023) used a similar approach however, they use a limit of $2 \times 10^9 \text{ eVcm}^{-2}\text{s}^{-1}\text{sr}^{-1}$. Furthermore, to counter problems due to orbital bias and make a data set that can be statistically compared to the others mentioned in the prior subsections, the threshold is used to create a binary data set of spacecraft locations (for several DMSP satellites) defined as being within either auroral or non auroral precipitation. From this data set statistical maps of auroral precipitation occurrence probability are then created.

2.6. Newell Coupling Function ϵ_N

We make use of the Newell coupling function

$$\epsilon_N = \frac{v^{4/3}}{1000} \left(\sqrt{B_y^2 + B_z^2} \right)^{2/3} \sin^{8/3}(\theta/2), \quad (1)$$

throughout this study. Here v , B_y , B_z , and $\theta = \tan^{-1}(B_y/B_z)$ are respectively the solar wind speed, the y and z components of the interplanetary magnetic field (IMF), and the IMF clock angle, with all quantities given in geocentric solar magnetic coordinates.

We use ϵ_N averaged over a two-hour backward-looking window, $\bar{\epsilon}_N$, as an indicator of solar wind driving. This quantity is calculated using solar wind and IMF measurements from the NASA OMNI database at one-minute resolution (King & Papitashvili, 2005). ϵ_N can range from 0 to over 160 and is highly correlated with the auroral electrojet geomagnetic index. Typical values are within the range 0–5.1 which makes up around 50% of the time.

3. Results

3.1. Conjunctions

In this section we present two conjunction events between DMSP satellites, *Swarm* satellites and the 105° magnetic meridian, on which the ground based magnetometer (GBM) electrojet boundary data set is located.

Figure 1 shows a conjunction between the 105° magnetic meridian, the *Swarm* A and C satellites and the DMSP F17 satellite for the period between 14:33:00 and 14:53:00 on 13th March 2014. Figure 2 shows a conjunction between the 105° magnetic meridian, the *Swarm* A satellite and the DMSP F18 satellite between 16:14:22 and 16:37:34 on the 22nd of February 2014. The middle right panel shows several sheet current density profiles, one for each satellite in the event. Each profile is constructed by finding the median sheet current density in S. J. Walker, Laundal, Reistad, Hatch, et al. (2023) occurring at times between when the two boundaries were identified by the particular satellite. Thus there are three median profiles in Figure 1 and two median profiles in Figure 2 each with associated boundaries.

In both conjunctions we find a clear similarity between the SECS derived eastward current, based on ground magnetometers, and the line current derived eastward currents, based on *Swarm* magnetometers. Unsurprisingly, we also see that the boundaries from the two electrojet data sets are very similar particularly if one considers the separation of the data points for the GBM electrojet boundaries, approximately 0.65° MLat. In both conjunctions we find the DMSP poleward boundary to coincide with the poleward electrojet boundaries, but the equatorward boundary is situated close to the peak of the electrojet. The equatorward extent of the integrated ion flux above the threshold matches well with the equatorward boundary of the electrojet, but the poleward extent only matches with the poleward boundary of the electrojet in Figure 1. Despite the short time scale of the conjunctions, the electrojet is not constant. In Figure 1 there is approximately 10 minutes separation between the boundaries produced by *Swarm* A and C. Both the associated median GBM current and *Swarm* based magnetometer (SBM) current show clear differences, but the GBM and SBM poleward boundaries are relatively stable over this time period. However, the *Swarm* C and DMSP F17 boundaries are approximately two minutes apart which is why they have near identical median GBM current profiles and the boundaries found from these current profiles are identical. In Figure 2 the *Swarm* A and DMSP F18 boundaries are approximately 10 min apart which may contribute to significantly different median GBM current profiles and clear differences in the equatorward GBM boundary. But, once again, the poleward boundary shows stability over this period and is identical for the median GBM current profiles associated with DMSP F18 and *Swarm* A.

3.2. Data Availability and Distribution

In the following section we present and describe a statistical investigation of the various boundary data sets.

To separate the data set by solar wind driving conditions for the purpose of statistics we bin the boundary data sets by $\bar{\epsilon}_N$, as described in Section 2.6. The $\bar{\epsilon}_N$ bins have been chosen so that the number of GBM electrojet boundaries is similar in each bin. Six bins have been created: $0 < \epsilon_N < 2.4$, $2.4 < \epsilon_N < 3.9$, $3.9 < \epsilon_N < 5.1$, $5.1 < \epsilon_N < 6.7$, $6.7 < \epsilon_N < 9.1$ and $\epsilon_N > 9.1$. The final bin ($\epsilon_N > 9.1$) is omitted due to its large range and having comparatively more anomalous data. The IMAGE boundaries are selected when there are at least four boundaries available for an image, to avoid spurious boundaries. In addition to the algorithm described in Section 2.1.2, the GBM electrojet boundaries are further screened to ensure confidence in the boundaries we present: (a) For each minute of data in S. J. Walker et al. (2022) the electrojet boundaries are defined as the boundaries identified for the strongest current section (where strength is defined as the absolute total current of the section). (b) The boundaries of the electrojet are checked for their proximity to the edge of the meridian, those occurring on the first three data points of the meridian (less than 50.5° MLat) and the last three data points (greater than 79.5° MLat) are removed to ensure that the boundary of the electrojet can be seen in S. J. Walker et al. (2022). (c) When an eastward electrojet is chosen the peak must be larger than 0.05 A/km and for a westward electrojet the peak must be below -0.1 A/km. (d) Finally, to make the boundaries comparable to those produced by Chisham et al. (2022) we bin the electrojet boundaries using MLT bins of width 1 MLT, centered at half MLTs.

In this subsection we present how the amount of data from each boundary data set and how the median absolute deviation (MAD) varies due to MLT. We focus on one bin: $5.1 < \bar{\epsilon}_N < 6.7$, as it in general shows the features we wish to highlight in this section. Furthermore, differences between the bins for the counts and the MAD is overall minimal. We make it clear when this is not the case and carefully describe the differences between the bins.

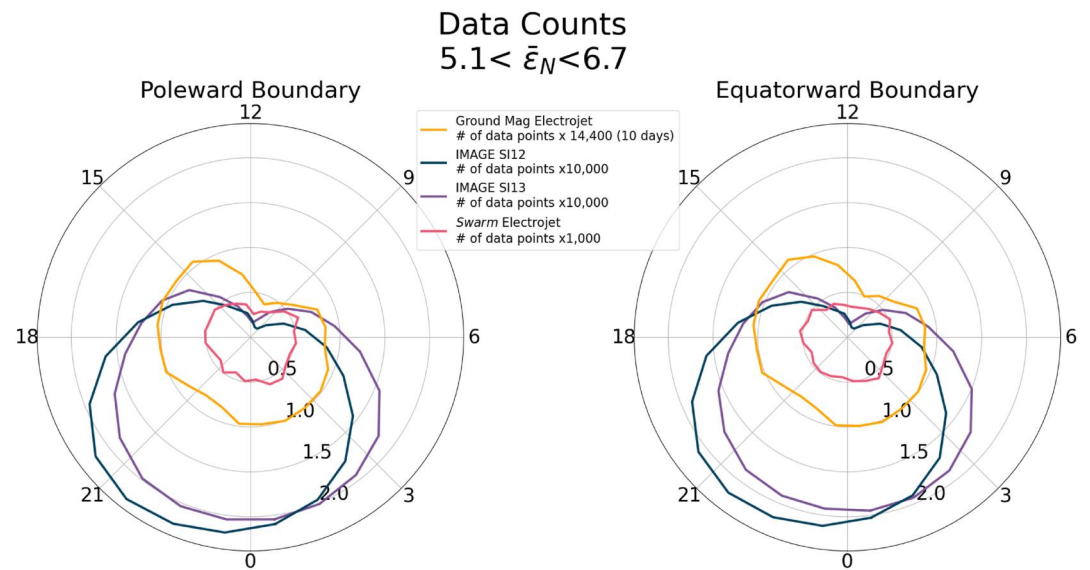


Figure 3. Data coverage and distribution of the S112, S113, Swarm based magnetometer electrojet and ground based magnetometer (GBM) electrojet boundaries within $5.1 < \bar{\epsilon}_N < 6.7$. The radial value indicates the amount of data in each MLT sector and is normalized for each data set as indicated by the legend. The GBM data set can be expressed in terms of time by incorporating its 1-min resolution. The left panel shows the data distribution for the poleward boundary and the right panel shows the data distribution for the equatorward boundary.

Figure 3 shows the number of poleward and equatorward boundaries that contribute to the $5.1 < \bar{\epsilon}_N < 6.7$ bin for all data sets. The normalization used in the Figure differs for each data set. This is necessary as there is a large difference in the time span of each data set (see Table 1) and consequently greatly different amounts of total data. The normalization allows us to more easily compare the MLT trends between the different data sets. The general MLT trend is not greatly different between the different $\bar{\epsilon}_N$ bins and thus the following description of the Figure can easily be applied to the other bins unless we state otherwise. There are many fewer SBM boundaries compared to other data sets and all four data sets show a reduction in the number of boundaries pre-noon, however this reduction is much more significant with the FUV boundaries. The difference in the counts between the poleward and equatorward boundaries is minimal for all data sets. There is also a reduction in the number of GBM boundaries between 20 and 23 MLT and, although we do not show these plots, a similar behavior can be observed for weaker $\bar{\epsilon}_N$ for the SBM boundaries.

Figure 4 shows the MAD of the poleward and equatorward boundaries, as the radial value (in degrees), for the same $\bar{\epsilon}_N$ range as used in Figure 3, in order to depict the spread of the distribution behind each statistic. In general, including the bins not shown, the MAD of the poleward and equatorward boundary for the electrojet boundaries are very similar, particularly in terms of the location of the peaks. The same cannot be said for the MAD of the S112 and S113 boundaries which exhibit peaks at 15 and 18 MLT respectively for the equatorward boundary but no clear peaks for the poleward boundary. Furthermore, the peaks in the MAD of the poleward and equatorward boundary for all data sets is consistent across all bins of $\bar{\epsilon}_N$. Overall the FUV boundaries have a smaller MAD than the other data sets, most significantly where the MAD peaks in GBM and SBM boundaries between 9 and 12 MLT and 20 and 23 MLT. However the MAD of the equatorward boundaries is comparable between 14 and 18 MLT and between 3 and 9 MLT and where the MAD of the FUV poleward boundaries peak their MAD is the largest of the data sets.

In summary, Figure 4 shows that the MAD is less than 3° for all electrojet boundary data sets, with the exception of the MAD for the poleward GBM electrojet boundary, which extends to nearly 3.5° around 21 MLT.

3.3. The Dependence of Average Boundaries on Solar Wind Coupling

We now present and describe the statistical maps (median values) of the different boundary data sets introduced in Section 2.

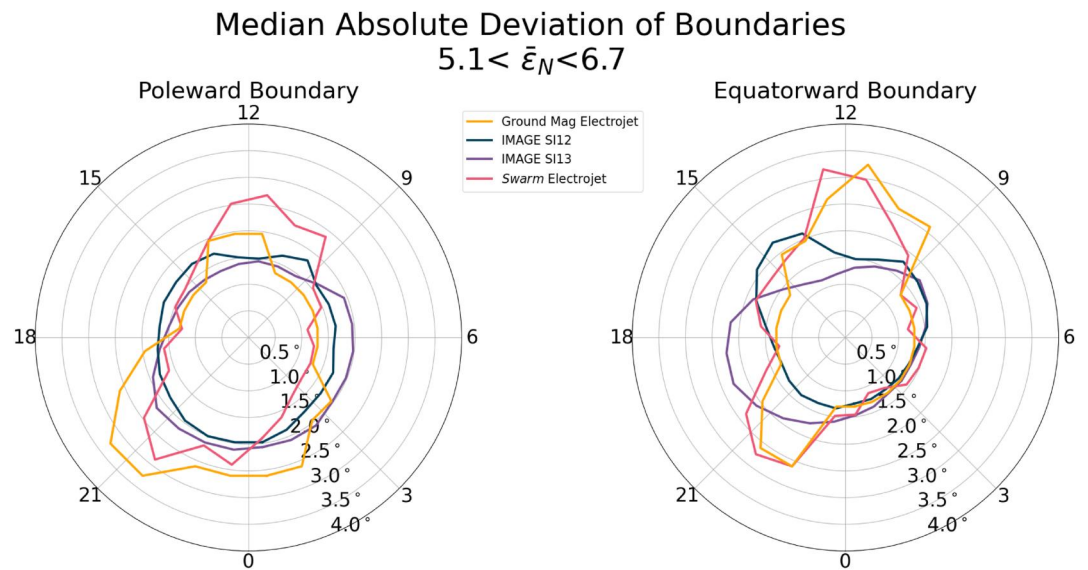


Figure 4. The median absolute deviation (MAD) in each MLT sector for the SI12, SI13, Swarm based magnetometer electrojet and ground based magnetometer electrojet boundaries within $5.1 < \bar{\epsilon}_N < 6.7$. The radial value indicates the MAD in degrees of MLat.

Figure 5 shows the median equatorward and poleward auroral boundaries using the SI12 and SI13 imagers on IMAGE (Chisham et al., 2022) as blue and purple lines respectively, together with the median GBM electrojet boundaries (this study) shown with orange lines. The auroral occurrence probability based on the SSJ instrument

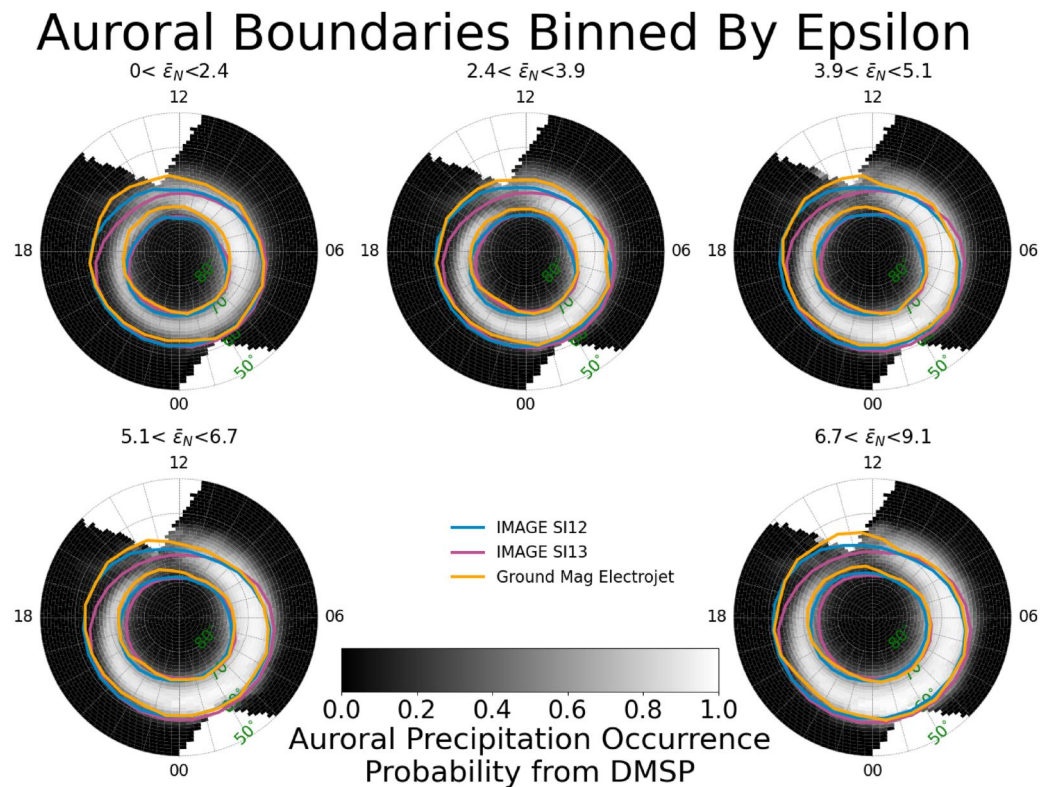


Figure 5. Median SI12, SI13 and ground based magnetometer electrojet boundaries in 5 bins of $\bar{\epsilon}_N$ (see Section 2.6) and in 24 MLT bins of size 1 hr, with the first bin being 0–1 MLT. The background color is used to show the auroral precipitation occurrence probability found by Decotte et al. (2023) and using their spatial bins and additionally binned by our $\bar{\epsilon}_N$ ranges.

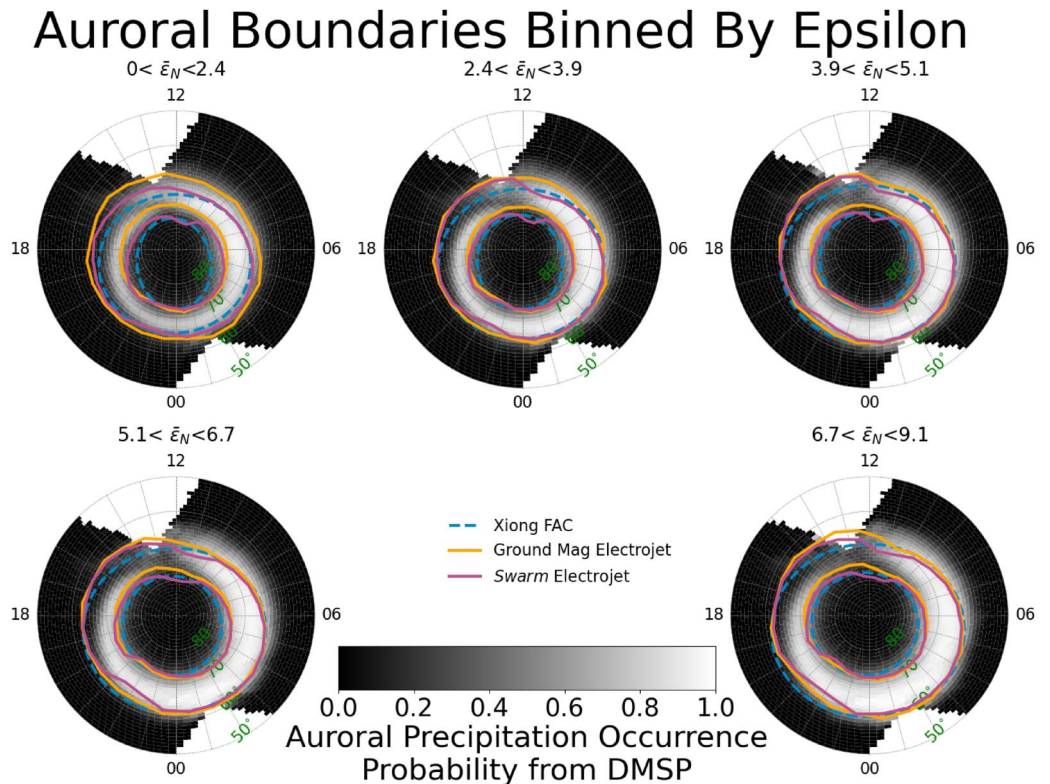


Figure 6. Constructed the same as Figure 5 but using Swarm based magnetometer electrojet boundaries instead of SI12 and SI13. Additionally, field-aligned current boundaries are found for each $\bar{\epsilon}_N$ bin by using the midpoint of the bins as input for the model (Xiong & Lühr, 2014).

onboard the DMSP satellites (Decotte et al., 2023; Kilcommons et al., 2017) is shown in gray-scale. Each plot within the Figure represents a different $\bar{\epsilon}_N$ bin, which we introduced in the previous subsection. Additionally, we have used bootstrapping to calculate how well defined the median of the data sets are. This is done using the scipy bootstrap function (Virtanen et al., 2020) where the use of default values creates 9,999 random realizations of the data (all the data that contributes to one median data point in Figure 5) each the same size as the initial data. The median is then found for each realization producing 9,999 realizations of the median and then the standard deviation is calculated using these medians which we refer to as the bootstrapped standard deviation of the median from hereafter. We do not show the bootstrapped standard deviation of the median as the values are small. SBM has the largest bootstrapped standard deviations of all the data set but, even so, the values do not exceed half a degree and therefore the medians of each data set can be considered well defined. However this should not be considered an indication of the spread of the distributions of the data sets, which is quantified by the MAD values in Figure 4, and further explored in Section 4.

We see a remarkable similarity between the SI12 boundaries and the electrojet boundaries in most MLT sectors. However, differences are apparent in the pre-midnight sector and around 15 MLT. In general for both boundaries SI12 is closer to the electrojets in comparison to the auroral occurrence probability and SI13. As $\bar{\epsilon}_N$ increases, the difference between SI12 and electrojet boundaries reduces in a region centered around 15 MLT. The MLT extent of this region also reduces as $\bar{\epsilon}_N$ increases. In the pre-midnight sector there is a weak trend of increasing difference between the SI12 and the electrojet boundaries with increasing $\bar{\epsilon}_N$. In the pre-midnight sector the SI12 boundaries remain quasi circular but the GBM boundaries deviate to higher latitudes. This causes the boundaries to deviate from a circular path toward a straighter one in Figure 5. This becomes more noticeable, and occurs on a larger range of MLTs, as $\bar{\epsilon}_N$ increases.

Figure 6 shows median boundaries for the GBM electrojets and the SBM electrojets, as purple and orange lines respectively, using the same MLT and $\bar{\epsilon}_N$ bins as in Figure 5. The same auroral occurrence probability maps are also shown. The FAC boundary model (Xiong & Lühr, 2014) is shown as a blue dashed line, where the midpoint

Seasonal Variation in Boundaries $5.1 < \bar{\epsilon}_N < 6.7$

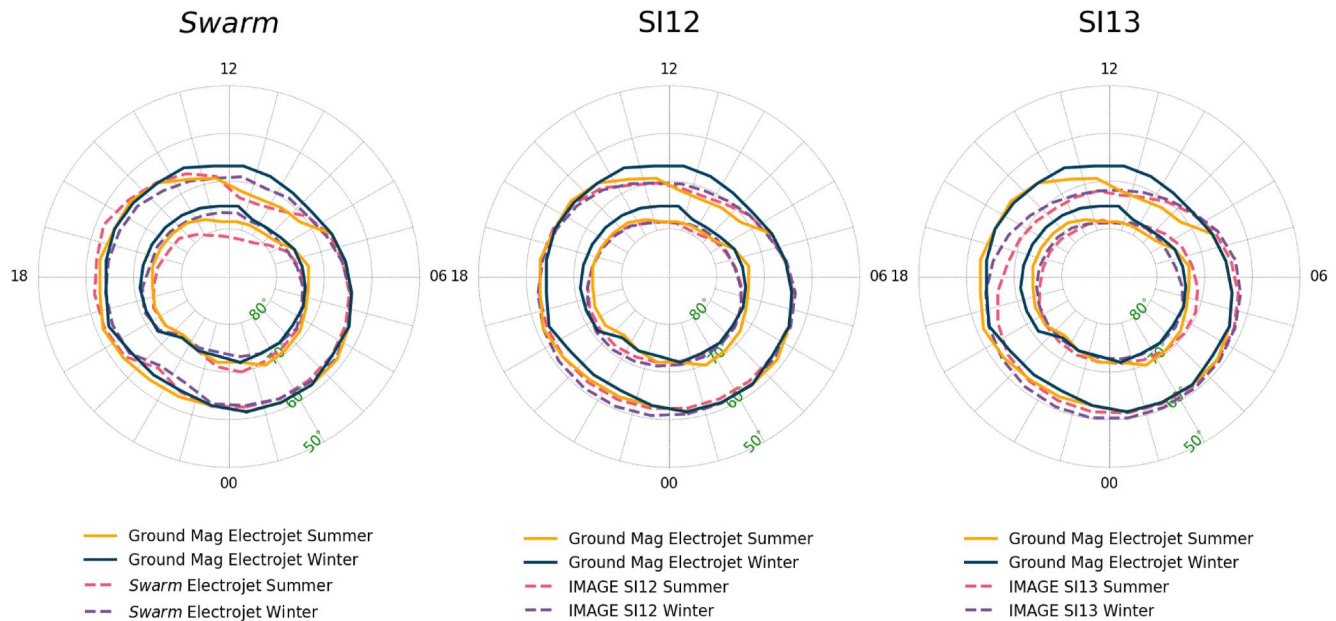


Figure 7. Median SI12, SI13, Swarm based magnetometer (SBM) electrojet boundaries compared with the ground based magnetometer (GBM) electrojet boundaries within one $\bar{\epsilon}_N$ bin from Figures 5 and 6 and using the same MLT bins. Boundaries are additionally binned into summer and winter, where summer is defined as when the dipole tilt is greater than 10° and winter is defined as when the dipole tilt is less than -10° . The left panel compares the seasonally binned GBM and SBM electrojet boundaries. The middle panel compares the seasonally binned GBM electrojet boundaries and the SI12 boundaries. The right panel compares the seasonally binned GBM electrojet boundaries and the SI13 boundaries.

of the $\bar{\epsilon}_N$ bin is used as input for the model. As stated previously the bootstrapped standard deviation of the data sets presented are small and thus the median boundaries in Figure 6 are well defined.

The different electrojet boundary data sets show a significant similarity for most MLT and $\bar{\epsilon}_N$ bins but the largest deviations appear on the night side for the poleward boundary and increase with $\bar{\epsilon}_N$. The equatorward boundary of the FAC boundary model shows similarities with the electrojet boundary data sets, however much like FUV boundaries in Figure 5 the FAC and electrojet boundaries are a poorer match in the pre-midnight sector where the shape of the electrojet boundaries change. In general the comparison is much worse between the FAC model and the electrojet boundaries for weaker $\bar{\epsilon}_N$, even more so for the poleward boundary than the equatorward boundary.

3.4. Seasonal Variability of Median Boundaries

Using satellite based FUV images and measurements of particle precipitation, previous studies have investigated how season affects the auroral oval (Oznovich et al., 1993), the OCB (Laundal et al., 2010), and the equatorward boundary of the diffuse aurora (Landry & Anderson, 2019). In this section we investigate how the different boundary data sets used in this study vary with season. We define season using the tilt of the Earth's dipole axis (ψ). This is the tilt of the dipole axis in terms of the Sun-Earth line where 0° is when the dipole axis is at a right angle with Sun-Earth line. A positive tilt is toward the Sun and a negative tilt is away (Laundal & Richmond, 2017). We define summer as $\psi > 10^\circ$ and winter as $\psi < -10^\circ$, since we only use data from the Northern hemisphere.

Figure 7 shows the median of the poleward and equatorward boundary for each boundary data set, using the same MLT binning used in Figure 5 and the $5.1 < \bar{\epsilon}_N < 6.7$ bin from the same Figure. From left to right the panel compares seasonal GBM electrojet boundaries with SBM electrojet boundaries, SI12 boundaries and SI13 boundaries respectively, where winter is defined as when the dipole tilt is less than -10° and summer when the dipole tilt is greater than 10° . We have also calculated the bootstrapped standard deviation for the median

boundaries shown, finding that they are typically less than 0.6° across all data sets for both summer and winter and the poleward and equatorward boundaries. Once again the SBM boundaries have the largest bootstrapped standard deviation but even the larger spikes do not exceed one degree. Since the GBM data set is from a fixed geographic location, it has its own inherent dipole tilt relation for a given MLT location, leading to systematic dipole tilt variations in MLT within the allowed summer/winter range. Additionally there exist biases within the distribution of each magnetometer's availability per month that can shift the median month in summer and winter away from the solstices. Hence, subtle seasonal differences should be interpreted with care. The GBM equatorward boundary shows little difference due to season at dawn and from 14 to 17 MLT. However, significant differences can be seen from 8 to 14 MLT and pre-midnight. The GBM poleward boundary shows seasonal differences at all MLT sectors, being closest around 5 MLT and most different around 17 MLT.

In the left panel we can see how the GBM and SBM boundaries compare seasonally. The SBM equatorward and poleward boundaries are similarly affected by season as the GBM boundaries are, in particular we see around 5 MLT that even the different data sets show little difference for both the poleward and equatorward boundaries. In other sectors the data sets are not as good a match. However, the seasonal trend is much the same, where the electrojet is more poleward during the summer in the pre-noon sector and more equatorward from 18 to 24 MLT. The pre-noon sector shows a clear shift in the equatorward boundary of the electrojet during the summer, deviating from the more circular path that is visible during the winter. There is a similar behavior for the SBM poleward boundaries but not so clearly for the GBM poleward boundaries, an effect that could be attributed to the latitudinal limit of the data sets as the median poleward boundary for the SBM data set is beyond the latitudinal extent of the GBM data set.

In the middle panel there is minimal seasonal variation in the SI12 poleward and equatorward boundaries. Therefore, although during summer the SI12 boundaries are similar to the GBM boundaries, in the winter they are not. The biggest difference between the SI12 and GBM equatorward boundaries occurs pre-noon and pre-midnight in both seasons. For the poleward boundary the biggest difference occurs between 11 and 20 MLT during the winter and 13 to 20 MLT in the summer.

In the right panel we see that SI13 has a greater seasonal variation in both boundaries than for SI12. For the equatorward boundary the greatest seasonal variation occurs from noon to midnight but from midnight to noon for the poleward boundary. Although the GBM boundaries do not match as well with SI13 as they do with SI12, there are some MLT sectors where the seasonal trends agree. In the SI12 and 13 data sets in the summer the equatorward boundary pre-noon exhibits a poleward shift and the poleward boundary has a poleward shift from 13 to 21 MLT and an equatorward shift between 1 and 6 MLT.

4. Discussion

Knowledge of the location of auroral oval boundaries is an important tool for understanding space weather and solar wind - magnetosphere coupling (Chisham et al., 2008). In particular, knowledge of the location of the OCB is very useful (Chisham, 2017), and a global and continually available proxy of the OCB would be invaluable. There are challenges associated with finding these boundaries through more conventional measurements such as auroral images and particle precipitation measurements. Here, we have proposed the advantages of understanding the auroral oval through the auroral electrojets due to the temporal and spatial prevalence of ground based magnetometers. In this section we discuss the results presented in Section 3, with a focus on how our electrojet boundary data set compares both statistically and in case studies to *Swarm*-based magnetometer electrojet boundaries (Kervalishvili et al., 2020; Viljanen et al., 2020) and other common means of estimating the auroral oval (SI12, SI13 and auroral precipitation occurrence probability) (Chisham et al., 2022; Decotte et al., 2023; Kilcommons et al., 2017).

In Figure 6 we presented the modeled FAC boundaries (Xiong & Lühr, 2014) together with the median electrojet boundary and auroral occurrence probability maps. One must be careful when interpreting differences between the FAC boundary model, the median boundaries and auroral occurrence probability because the $\bar{\epsilon}_N$ used to constrain the model and the $\bar{\epsilon}_N$ used to bin the boundary data are calculated through different methods (Xiong & Lühr, 2014). Despite this, the trend of increasing eccentricity of the poleward and equatorward boundaries as $\bar{\epsilon}_N$ weakens remains a valid similarity between the FAC boundaries and the SBM and GBM electrojet boundaries. Due to the latitude limit of the GBM electrojet boundaries the increase in eccentricity is clearer for the SBM electrojet poleward boundary than the GBM electrojet poleward boundary. Excluding regions affected by the pre-

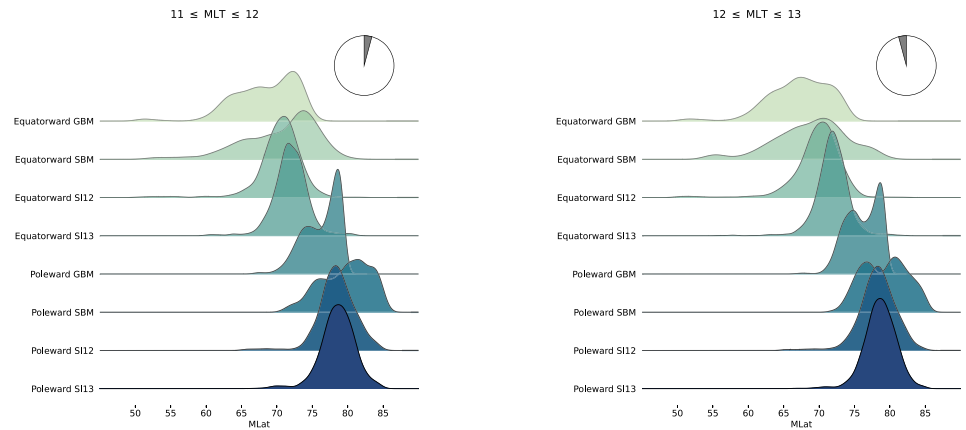
noon and pre-midnight electrojet discontinuities, it is likely that an ellipse would represent an appropriate geometry for an electrojet boundary model and a similar approach to Xiong and Lühr (2014) could be a fruitful endeavor.

The SBM and GBM electrojet boundaries are similar both statistically (Figure 6) and in the two conjunction studies we present in Section 3.1 (Figures 1 and 2). However, at the electrojet discontinuities, around pre-midnight and pre-noon (regions surrounding and including the location of convection reversal), the SBM and GBM electrojet are dissimilar from each other and from the SI12 and SI13 boundary data sets. It is in these regions that we also observe spikes in the MAD of both boundaries from the SBM and GBM data sets (Figure 4), and a dip in the counts (Figure 3). Johnsen (2013) comments on the challenges of determining the electrojet boundaries at these discontinuities due to the elevated complexity of the current systems, and omits these regions from their boundary determination using three- and four-hour universal time windows for the pre-noon and pre-midnight discontinuities, respectively. However, we see in Figure 5 that the median electrojet boundaries deviate more from the auroral oval (as defined by SI12) for an increasing range of MLTs with increasing $\bar{\epsilon}_N$ value. This suggests that a fixed window is not suitable and that in many cases useful information about the boundaries is likely discarded.

To understand how different boundary data sets are behaving in the discontinuity regions, we present in Figure 8 the full distribution of the boundaries in two MLT bins around magnetic noon (11–12 MLT and 12–13 MLT) and two MLT bins around pre-midnight (20–21 and 21–22 MLT) for a single $\bar{\epsilon}_N$ bin (5.1–6.7) from Figure 5. There are two peaks in the distribution of GBM and SBM electrojet boundaries, most prominent in the distribution of poleward boundaries, which suggests two distinct populations. Figure 9 is a simplified description of the east–west vector of the divergence-free currents in the auroral zone. In this Figure we depict what we believe is the likely cause of the bimodal distribution in the GBM and SBM electrojet boundaries in certain MLT sectors. Either side of the discontinuities the strongest current sections are in opposite directions. For the Harang Discontinuity (HD) (green shaded region at 24 MLT), westward of the discontinuity the eastward section of the current is strongest and our algorithm will describe the auroral oval using the boundaries of the eastward current section. Eastward of the HD the westward section of the current is strongest and our algorithm will use the boundaries of the westward current section. The opposite is the case for the dayside discontinuity (green shaded area at 12 MLT). Eastward of the discontinuity the eastward current section is dominant and westward of the discontinuity the westward current section is dominant. In all these cases the dominant current section is the lower latitude of the two current sections in Figure 9. With increasing proximity to the discontinuities the low latitude current section becomes weaker on average and the high latitude current section becomes stronger on average. At the discontinuity the eastward and westward current sections are on average of similar strength. This makes the dominant current section ambiguous. In our boundaries we observe this as the boundary distributions becoming more bimodal because the probability of selecting the high latitude or low latitude current section becomes increasingly similar. In Figure 6 we observe this as the median boundary shifting poleward with increasing proximity to the average location of the discontinuities due to the increase in the probability of selecting the high latitude current section.

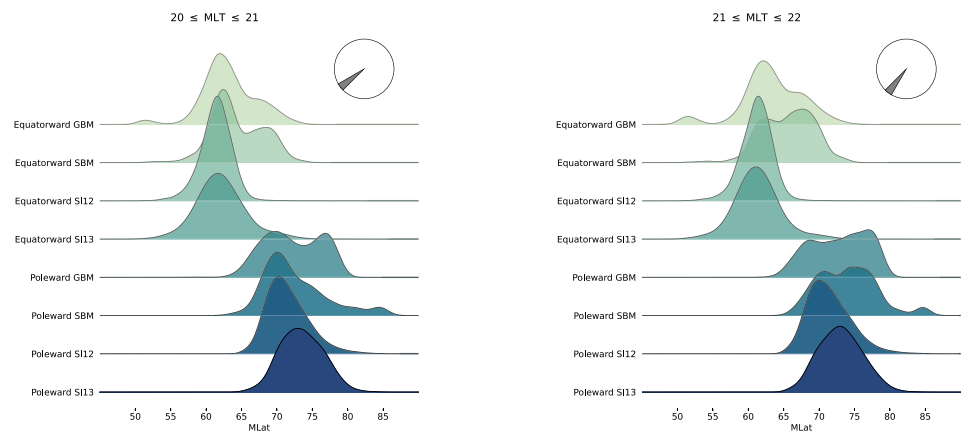
Given that ambiguity in the dominant current section causes a poleward shift in the average boundaries, we can use the poleward shift in the GBM and SBM electrojet boundaries in Figures 5 and 6 to identify where and how often the ambiguity occurs. SBM exhibits a greater poleward shift than the GBM data set and this is due to the latitude limitations of the GBM data set; a consequence of the latitude distribution of magnetometers used by S. Walker, Laundal, Reistad, Hatch, et al. (2023). We also see in Figure 6 that the ambiguity pre-midnight covers a greater range of MLTs than pre-noon, something that can be the result of a difference in the size of the HD and the dayside discontinuity or/and a difference in the distribution in the MLT location of the two discontinuities. The MLT of the discontinuity on the dayside is expected to depend on the IMF B_y , which strongly controls the plasma flow resulting from dayside reconnection (e.g., Laundal et al., 2018). Further separation by IMF B_y could shed light on the effect of B_y on the GBM/SBM poleward boundary variation. As we can see in Figure 7, the poleward shift in the boundaries at the dayside electrojet discontinuity is enhanced during the summer compared to the winter. However, there appears to be no significant seasonal variation in the effect in the HD region. This difference in seasonal variation between the dayside and the nightside could be an effect of corresponding variations in solar EUV produced conductance, which is more important on the dayside. In terms of the use of the GBM and SBM electrojet boundary data sets as auroral oval proxies one must consider the proximity to the HD and dayside

$$5.1 < \bar{\epsilon}_N < 6.7$$



(a) Boundary distributions between 11 and 12 MLT

(b) Boundary distributions between 12 and 13 MLT



(c) Boundary distributions between 20 and 21 MLT

(d) Boundary distributions between 21 and 22 MLT

Figure 8. Distribution of the poleward boundary and equatorward boundary for the SI12, SI13, Swarm based magnetometer electrojet and ground based magnetometer electrojet boundary data sets within one $\bar{\epsilon}_N$ bin from Figures 5 and 6. Four MLT bins are selected from Figures 5, 6, 11, 12 MLT (a), 12 to 13 MLT (b), 20 to 21 MLT (c), and 21 to 22 MLT (d).

discontinuity, solar wind driving ($\bar{\epsilon}_N$) and dipole tilt in order to determine the likelihood of dominant current section ambiguity.

In the HD we suggest the dominant current section ambiguity is the result of plasma convection creating two opposing current sections at different latitudes (as shown in Figure 9). Their similar strength makes the selection of the dominant current section inconsistent creating the two boundary populations shown in Figures 8c and 8d. The dominant current section ambiguity on the dayside could be explained in the same way. The two opposing current sections may also be created by the high latitude DPY current and the low latitude convection driven electrojet. The DPY current is known to be created by lobe reconnection and is consequently stronger during the summer compared to the winter and when the IMF is northward (Friis-Christensen & Wilhelm, 1975). This could explain the higher median electrojet boundaries in the summer compared to the winter that we see in Figure 7. However, ϵ_N depends on the IMF clock angle. During a perfectly northward IMF $\epsilon_N = 0$, it is highly improbable that the solar wind conditions would be such that the IMF has a significant northward component and have $5.1 < \epsilon_N < 6.7$ (the bin presented in Figure 7). There is a possibility that we must consider that the averaging scheme, used in Section 2.6, could result in boundaries being placed in the $5.1 < \bar{\epsilon}_N < 6.7$ bin despite being

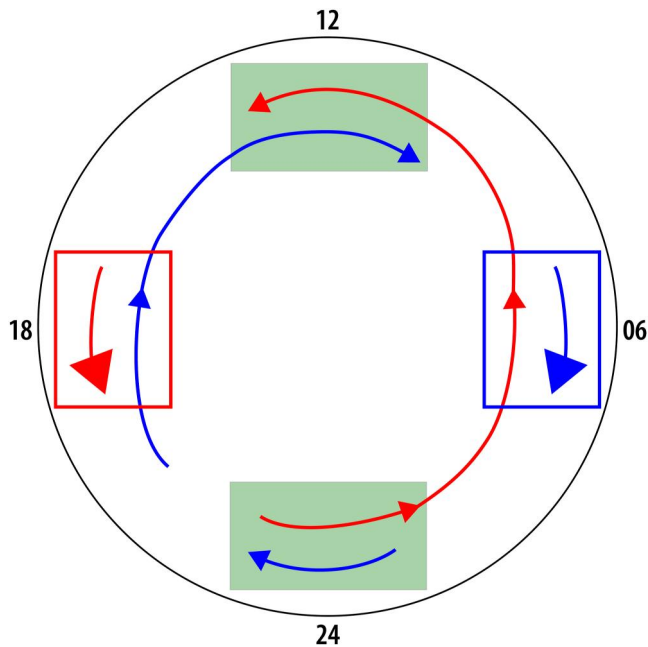


Figure 9. A simplified schematic of the electrojet currents. Blue arrows show the westward current and red arrows show the eastward current. In the red box the eastward current is dominant and the region is easily identified as an eastward electrojet using the methodology described in this paper. In the blue box the westward current is dominant and the region is easily identified as a westward electrojet. The green shaded areas show the electrojet discontinuities where the westward and eastward current are of similar strength. In these regions the direction of the dominant current will vary and the electrojet is not easily defined.

influenced by a northward IMF with a much smaller ϵ_N . This may arise due to a strong southward IMF also existing within the averaging window. An argument against DPY currents being the cause of the bimodal distribution of the GBM boundaries, in Figures 8a and 8b is the latitude limitations. We discard boundaries that are above 79.5° , therefore it is unlikely that we can resolve the full latitude extent of the DPY current in order to find the poleward boundary of it. This does not have a significant effect on the equatorward GBM boundary and may explain why we see a greater difference in latitude from summer to winter for the median equatorward GBM boundary than we do for the median poleward. The SBM boundaries support this as they do not have this latitude limitation and show a similar shift in the median poleward and equatorward boundaries from summer to winter. While DPY currents may explain this seasonal variation in the boundaries it does not fully explain the bimodal boundary distributions (Figures 8a and 8b). The bimodal distribution is most visible in the poleward boundary for both the SBM and GBM boundary data sets. If we assume that the DPY currents are responsible for the seasonal variation in the electrojet boundaries and are responsible for the bimodal distribution then the bimodal nature should be equally clear for both poleward and equatorward SBM boundaries. For the GBM boundaries the equatorward boundary distribution should be more clearly bimodal than the poleward boundary. Neither of these situations is the case. Considering this and our discussion about ϵ_N , we must conclude that it is unlikely that the bimodal distribution on the dayside is solely or primarily due to the DPY currents. Furthermore, without further information it is logical to assume that the cause of the bimodal distribution on the dayside is the same as the cause of the bimodal distribution in the HD. Although out of the scope of this study, sorting by the polarity and strength of IMF B_y along with season and the polarity of IMF B_z may shed light on the impact of the DPY currents on the identification of the electrojet at the dayside discontinuity.

When analyzing Figure 5 we find that the GBM electrojet boundaries, in most MLT sectors, are as close to the SI12 boundaries as they are to the SBM electrojet boundaries, particularly as $\bar{\epsilon}_N$ increases. On the other hand, the SI13 boundaries are only close when the differences between SI12 and SI13 are small. Feldstein et al. (1999) found that the eastward electrojet often extends equatorward of the auroral oval as defined by electron precipitation; this is the same relationship that we observe between the electrojet boundaries and the SI13 boundaries and the auroral occurrence probability. Given that SI12 measures the emissions related to proton precipitation and SI13 measurements are dominated by emissions related to electron precipitation (Coumans et al., 2004; Frey et al., 2001; Gérard et al., 2001), our results and the results of Feldstein et al. (1999) therefore support one another, and contradict the notion that the electrojets must flow within the auroral oval as defined by electron precipitation (Rostoker et al., 1996).

Although SI13 is related to the precipitation of auroral energy electrons, Figure 5 shows that the auroral precipitation occurrence probability maps do not everywhere align well with the SI13 boundaries, in particular in the pre-noon sector where the auroral precipitation occurrence probability extends far equatorward of all the boundary data sets in this study. In general the SI13 boundaries and the auroral precipitation occurrence probability become more dissimilar for weaker $\bar{\epsilon}_N$ values but the opposite is the case in the pre-noon sector. Figures 1 and 2 occur in the MLT ranges 16.5–16.9 and 18.2–18.6 and with $\bar{\epsilon}_N$ ranges of approximately 3.6–4.3 and 5.4–6.1, respectively.

Although Feldstein et al. (1999) do not examine the latitude limits of auroral energy proton precipitation they do comment on the peak in proton precipitation occurring close to the center of the eastward electrojet. Similarly, in Figures 1 and 2 we find the center of enhanced auroral energy proton precipitation occurs around the center of the eastward electrojet. Both in the median boundaries (Figure 5) and in the first conjunction (Figure 1) we observe an extension of the relationship between the eastward electrojet and proton precipitation, where limits of the precipitation are close to or coincident with the eastward electrojet boundaries. Figures 1 and 2 show the same as Feldstein et al. (1999) and the median boundaries, that the eastward electrojet can extend equatorward of the

electron precipitation defined auroral oval. However, the poleward limit of the electron precipitation occurring close to the poleward boundary of the eastward electrojet that can be seen in Figures 1 and 2 is not shown in Figure 5 or in Feldstein et al. (1999) but is seen for the westward electrojet in Figure 5 and Feldstein et al. (1999). Finally, in Figure 2 the latitudinal extent of the proton precipitation poorly reflects the electrojet boundaries. Despite this, the equatorward boundary of the proton precipitation is much closer to the electrojet boundary than for the electron precipitation. Feldstein et al. (1999) finds a large variation in the relationship between precipitation regions and boundaries and the electrojet boundaries and centers; something that is also clear in this study with the difference between patterns in the average boundaries (Figure 5), and the direct comparisons (Figures 1 and 2). A greater number of direct comparisons may be required to ensure the trends in the average boundaries are representative of the true relationship between the different boundaries. In summation, with the results presented one must be careful when interpreting the auroral oval boundaries derived from the electrojet boundaries based on what is seen in the trends of the average boundaries.

5. Conclusion

Finding the boundaries of the auroral oval is of key importance in the study of the solar wind-magnetosphere coupling. The region they define informs us where the majority of the energy from this coupling is deposited, which in turn can enable the development of improved models aiding the identification and mitigation of space weather hazards. Of particular importance is the OCB which allows us to quantify the amount of open flux in the polar cap and subsequently understand the amount of energy stored in the magnetotail. In this study we have developed an algorithm that, among other properties, detects the boundaries of the auroral electrojets. Taking advantage of the eastward sheet current density profiles produced by S. Walker, Laundal, Reistad, Hatch, et al. (2023), we have created a data set through the use of our algorithm that spans 20 years and, due to data gaps, totals 11 years with 1-min cadence. We make this data set publicly available due to the large range of applications that go beyond the scope of this paper.

The goal of our study was to understand the feasibility of an auroral oval boundary proxy based on our electrojet boundaries. We have found that the auroral oval described through proton and electron precipitation, and their associated FUV aurora, can be variable. Even the average electron-defined auroral oval is shown to have significant differences depending on if it is located using S113 images or measurements of electron precipitation. We find that the electrojet boundaries have a very different relationship with the proton auroral oval than they do with the electron auroral oval: the proton precipitation auroral oval boundaries are more closely coincident with the electrojet boundaries, while the auroral electrojets can flow outside the electron precipitation auroral oval as also shown by Feldstein et al. (1999). However, as the auroral oval is more typically described by electron precipitation (Feldstein & Starkov, 1967; Kilcommons et al., 2017; Newell et al., 1996), this fact is contrary the typical description of the boundaries of the auroral zone.

If we move to the paradigm of describing the auroral oval through proton precipitation we can see that there is indeed on average a close resemblance between the auroral oval and the electrojet boundaries. However, determination of the auroral oval from the electrojet boundaries encounters three key challenges: (a) Increasing dominant current section ambiguity with proximity to the electrojet discontinuities makes electrojet boundaries in the pre-noon and pre-midnight sectors a very poor proxy of the auroral oval. (b) The similarities between the electrojet boundaries and the auroral oval boundaries show a seasonal and reconnection rate ($\bar{\epsilon}_N$ value) dependence. (c) While the auroral oval and electrojet boundaries are statistically similar, analysis of conjunctions shows that even under favorable conditions and locations the truth does not always match the average.

Finally, while we are not the first to find the electrojet boundaries on a routine basis (Johnsen, 2013; Viljanen et al., 2020), we are the first to provide a publicly available data set that is based on ground magnetometers with a significant temporal advantage over those produced from measurements by the *Swarm* satellites. The global shape of the electrojet and its relationship with the auroral oval shows to be an important property of polar ionospheric dynamics and simply reducing the electrojet to singular values, such as the AL and AU indices, will significantly hinder understanding of this field (Kamide & Akasofu, 1983; Rostoker et al., 1980) and limit the capabilities of interpreting the auroral oval when global FUV images are not available or are ineffective.

Data Availability Statement

The solar wind and interplanetary magnetic field measurements has been downloaded from the OMNI database: OMNI Solar Wind Data (2023). The data set of divergence-free sheet current density profiles used in the electrojet algorithm to estimate the ground based magnetometer electrojet boundaries can be found at S. J. Walker et al. (2022). The data set of electrojet boundaries and properties created in this study can be found at S. J. Walker, Laundal, Reistad, Hatch, et al. (2023). The BAS-derived IMAGE auroral boundaries can be found at Chisham (2022). The data set of *Swarm* derived electrojet boundaries can be found through VirES for *Swarm* (2023) (Viljanen et al., 2020).

Acknowledgments

This work was supported by Research Council of Norway under contracts 223252/F50 and 300844/F50 and by the Trond Mohn Foundation. GC was supported by the British Antarctic Survey Polar Science for a Sustainable Planet Programme, funded by the UK Natural Environment Research Council (NERC) as well as the UK NERC directed grant NE/V002732/1. The authors would like to thank those involved in producing the IMAGE boundary data sets: Peter Boakes, Nicola Longden, Angeline Burrell, Mervyn Freeman, Steve Milan, and Gary Abel. The original raw IMAGE FUV data were provided courtesy of the instrument PI Stephen Mende (University of California, Berkeley). We thank the PI, the IMAGE mission, and the IMAGE FUV team for data usage and processing tools. The raw image data, and software, were acquired from <http://sprg.ssl.berkeley.edu/image/>. We extend our gratitude to the members of the International Space Science Institute (ISSI) International Team project #506 Understanding Mesoscale Ionospheric Electrodynamics Using Regional Data Assimilation for the discussions and insight into the topic of study. We also thank ISSI Bern for hosting the team. In S. Walker, Laundal, Reistad, Hatch, et al. (2023) the divergence-free currents are estimated through ground based magnetometers and as such these measurements are integral to this current study. We therefore gratefully acknowledge: IMAGE, PI Liisa Juusola; DTU Space, PI Anna Willer; SGU, PI Jan Wittke; TGO, PI Magnar Johnsen; FMI; PI Liisa Juusola, IG PAS, Anne Neska and Jan Reda; SGO, Eija Tanskanen and Tero Raita; for the operation of the magnetometers. For the processing, baseline removal and distribution of the ground magnetometer data we acknowledge: SuperMAG, PI Jesper W. Gjerloev.

References

- Aakjær, C. D., Olsen, N., & Finlay, C. C. (2016). Determining polar ionospheric electrojet currents from *Swarm* satellite constellation magnetic data. *Earth Planets and Space*, 68(1), 1–14. <https://doi.org/10.1186/s40623-016-0509-y>
- Amm, O. (1997). Ionospheric elementary current systems in spherical coordinates and their application. *Journal of Geomagnetism and Geoelectricity*, 49(7), 947–955. <https://doi.org/10.5636/jgg.49.947>
- Amm, O., & Viljanen, A. (1999). Ionospheric disturbance magnetic field continuation from the ground to the ionosphere using spherical elementary current systems. *Earth Planets and Space*, 51(6), 431–440. <https://doi.org/10.1186/BF03352247>
- Andersson, L., Peterson, W. K., & McBryde, K. M. (2004). Dynamic coordinates for auroral ion outflow. *Journal of Geophysical Research*, 109(A8), 8201. <https://doi.org/10.1029/2004JA010424>
- Boakes, P. D., Milan, S. E., Abel, G. A., Freeman, M. P., Chisham, G., Hubert, B., & Sotiropolis, T. (2008). On the use of IMAGE FUV for estimating the latitude of the open/closed magnetic field line boundary in the ionosphere. *Annales Geophysicae*, 26(9), 2759–2769. <https://doi.org/10.5194/angeo-26-2759-2008>
- Bothmer, V., Bothmer, & Volker (2013). Affects - advanced forecast for ensuring communications through space. *EGUGA*, 15, 2013–11752. Retrieved from <https://ui.adsabs.harvard.edu/abs/2013EGUGA..1511752B/abstract>
- Burrell, A. G., Chisham, G., Milan, S. E., Kilcommons, L., Chen, Y. J., Thomas, E. G., & Anderson, B. (2020). AMPERE polar cap boundaries. *Annales Geophysicae*, 38(2), 481–490. <https://doi.org/10.5194/angeo-38-481-2020>
- Carbary, J. F. (2005). A Kp-based model of auroral boundaries. *Space Weather*, 3(10). <https://doi.org/10.1029/2005SW000162>
- Chisham, G. (2017). A new methodology for the development of high-latitude ionospheric climatologies and empirical models. *Journal of Geophysical Research: Space Physics*, 122(1), 932–947. <https://doi.org/10.1002/2016JA023235>
- Chisham, G. (2022). Ionospheric boundaries derived from IMAGE satellite mission data (May 2000–October 2002) – VERSION 2.0 (Version 2.0) [Dataset]. <https://doi.org/10.5285/fa592594-93e0-4ee1-8268-b031ce21c3ca>
- Chisham, G., Burrell, A. G., Thomas, E. G., & Chen, Y. J. (2022). Ionospheric boundaries derived from auroral images. *Journal of Geophysical Research: Space Physics*, 127(7). <https://doi.org/10.1029/2022JA030622>
- Chisham, G., Freeman, M. P., Abel, G. A., Lam, M. M., Pinnock, M., Coleman, I. J., et al. (2008). Remote sensing of the spatial and temporal structure of magnetopause and magnetotail reconnection from the ionosphere. *Reviews of Geophysics*, 46(1). <https://doi.org/10.1029/2007RG000223>
- Coumans, V., Gérard, J. C., Hubert, B., Meurant, M., & Mende, S. B. (2004). Global auroral conductance distribution due to electron and proton precipitation from IMAGE-FUV observations. *Annales Geophysicae*, 22(5), 1595–1611. <https://doi.org/10.5194/ANGEO-22-1595-2004>
- Decotte, M., Laundal, K. M., Hatch, S. M., & Reistad, J. P. (2023). Auroral oval morphology: Dawn-Dusk asymmetry partially induced by Earth's rotation. *Journal of Geophysical Research: Space Physics*, 128(6), e2023JA031345. <https://doi.org/10.1029/2023JA031345>
- Feldstein, Y. I., Gromova, L. I., Grafe, A., Meng, C. I., Kalegav, V. V., Alexeev, I. I., & Sumaruk, Y. P. (1999). Dynamics of the auroral electrojets and their mapping to the magnetosphere. *Radiation Measurements*, 30(5), 579–587. [https://doi.org/10.1016/S1350-4487\(99\)00219-X](https://doi.org/10.1016/S1350-4487(99)00219-X)
- Feldstein, Y. I., & Starkov, G. V. (1967). Dynamics of auroral belt and polar geomagnetic disturbances. *Planetary and Space Science*, 15(2), 209–229. [https://doi.org/10.1016/0032-0633\(67\)90190-0](https://doi.org/10.1016/0032-0633(67)90190-0)
- Frey, H. U., Mende, S. B., Carlson, C. W., Gérard, J. C., Hubert, B., Spann, J., et al. (2001). The electron and proton aurora as seen by IMAGE-FUV and FAST. *Geophysical Research Letters*, 28(6), 1135–1138. <https://doi.org/10.1029/2000GL012352>
- Friis-Christensen, E., & Wilhjelm, J. (1975). Polar cap currents for different directions of the interplanetary magnetic field in the Y-Z plane. *Journal of Geophysical Research*, 80(10), 1248–1260. <https://doi.org/10.1029/ja080i010p01248>
- Gérard, J. C., Hubert, B., Meurant, M., Shematovich, V. I., Bisikalo, D. V., Frey, H., et al. (2001). Observation of the proton aurora with IMAGE FUV imager and simultaneous ion flux in situ measurements. *Journal of Geophysical Research*, 106(A12), 28939–28948. <https://doi.org/10.1029/2001JA900119>
- Harang, L. (1946). The mean field of disturbance of polar geomagnetic storms. *Journal of Geophysical Research*, 51(3), 353–380. <https://doi.org/10.1029/te051i003p00353>
- Holzworth, R. H., & Meng, C. I. (1975). Mathematical representation of the auroral oval. *Geophysical Research Letters*, 2(9), 377–380. <https://doi.org/10.1029/GL002i009p00377>
- Johnsen, M. G. (2013). Real-time determination and monitoring of the auroral electrojet boundaries. *Journal of Space Weather and Space Climate*, 3, A28. <https://doi.org/10.1051/swsc/2013050>
- Juusola, L., Amm, O., & Viljanen, A. (2006). One-dimensional spherical elementary current systems and their use for determining ionospheric currents from satellite measurements. *Earth Planets and Space*, 58(5), 667–678. <https://doi.org/10.1186/BF03351964>
- Kamide, Y., & Akasofu, S. I. (1983). Notes on the auroral electrojet indices. *Reviews of Geophysics*, 21(7), 1647–1656. <https://doi.org/10.1029/RG021I007P01647>
- Kervalishvili, G., Stolle, C., Jan, R., & Kauristie, K. (2020). Data, innovation, and science cluster swarm-AEBS description of the processing algorithm. Technical Report. <https://earth.esa.int/eogateway/documents/20142/37627/Swarm-AEBS-processing-algorithm-description.pdf>
- Kilcommons, L. M., Redmon, R. J., & Knipp, D. J. (2017). A new DMSP magnetometer and auroral boundary data set and estimates of field-aligned currents in dynamic auroral boundary coordinates. *Journal of Geophysical Research: Space Physics*, 122(8), 9068–9079. <https://doi.org/10.1002/2016JA023342>

- King, J. H., & Papitashvili, N. E. (2005). Solar wind spatial scales in and comparisons of hourly Wind and ACE plasma and magnetic field data. *Journal of Geophysical Research*, *110*(A2), A02104. <https://doi.org/10.1029/2004JA010649>
- Kisabeth, J. L., & Rostoker, G. (1971). Development of the polar electrojet during polar magnetic substorms. *Journal of Geophysical Research*, *76*(28), 6815–6828. <https://doi.org/10.1029/ja076i028p06815>
- Landry, R. G., & Anderson, P. C. (2019). Empirical modeling of the equatorward boundary of auroral precipitation using DMSP and DE 2. *Journal of Geophysical Research: Space Physics*, *124*(3), 2072–2082. <https://doi.org/10.1029/2018JA025451>
- Laundal, K. M., Finlay, C. C., Olsen, N., & Reistad, J. P. (2018). Solar wind and seasonal influence on ionospheric currents from Swarm and CHAMP measurements. *Journal of Geophysical Research: Space Physics*, *123*(5), 4402–4429. <https://doi.org/10.1029/2018JA025387>
- Laundal, K. M., Østgaard, N., Snekvik, K., & Frey, H. U. (2010). Interhemispheric observations of emerging polar cap asymmetries. *Journal of Geophysical Research*, *115*(7), 7230. <https://doi.org/10.1029/2009JA015160>
- Laundal, K. M., & Richmond, A. D. (2017). Magnetic coordinate systems. *Space Science Reviews*, *206*(1–4), 27–59. <https://doi.org/10.1007/S11214-016-0275-Y/FIGURES/13>
- Longden, N., Chisham, G., Freeman, M. P., Abel, G. A., & Sotirelis, T. (2010). Estimating the location of the open-closed magnetic field line boundary from auroral images. *Annales Geophysicae*, *28*(9), 1659–1678. <https://doi.org/10.5194/ANGE0-28-1659-2010>
- Mende, S. B., Heeterds, H., Frey, H. U., Lampton, M., Geller, S. P., Habraken, S., et al. (2000). Far Ultraviolet imaging from the IMAGE spacecraft. 1. System design. *Space Science Reviews*, *91*(1–2), 243–270. <https://doi.org/10.1023/A:1005271728567/METRICS>
- Mende, S. B., Heeterds, H., Frey, H. U., Stock, J. M., Lampton, M., Geller, S. P., et al. (2000). Far ultraviolet imaging from the image spacecraft. 3. Spectral imaging of Lyman- α and OI 135.6 nm. *Space Science Reviews*, *91*(1–2), 287–318. <https://doi.org/10.1023/A:1005292301251/METRICS>
- Milan, S. E., Clausen, L. B., Coxon, J. C., Carter, J. A., Walach, M. T., Laundal, K., et al. (2017). Overview of solar wind–Magnetosphere–Ionosphere–Atmosphere coupling and the generation of magnetospheric currents. *Springer Netherlands*, *206*(1–4), 547–573. <https://doi.org/10.1007/s11214-017-0333-0>
- Milan, S. E., Provan, G., & Hubert, B. (2007). Magnetic flux transport in the Dungey cycle: A survey of dayside and nightside reconnection rates. *Journal of Geophysical Research*, *112*(A1), 1209. <https://doi.org/10.1029/2006JA011642>
- Newell, P. T., Feldstein, Y. I., Galperin, Y. I., & Meng, C.-I. (1996). Morphology of nightside precipitation. *Journal of Geophysical Research*, *101*(A5), 10737–10748. <https://doi.org/10.1029/95JA03516>
- Newell, P. T., Sotirelis, T., Liou, K., Meng, C. I., & Rich, F. J. (2007). A nearly universal solar wind–magnetosphere coupling function inferred from 10 magnetospheric state variables. *Journal of Geophysical Research*, *112*(1), 1206. <https://doi.org/10.1029/2006JA012015>
- Ohma, A., Madelaire, M., Laundal, K. M., Reistad, J. P., Hatch, S. M., Gasparini, S., et al. (2023). Background removal from global auroral images: Data driven dayglow modelling. *Earth and Planetary Physics*, *8*(1), 1–11. <https://doi.org/10.26464/EPP2023051>
- Olsen, N. (1996). A new tool for determining ionospheric currents from magnetic satellite data. *Geophysical Research Letters*, *23*(24), 3635–3638. <https://doi.org/10.1029/96GL02896>
- OMNI Solar Wind Data. (2023). Retrieved from https://cdaweb.gsfc.nasa.gov/sp_phys/data/omni/hro_1min/
- Oznovich, I., Eastes, R. W., Huffman, R. E., Tur, M., & Glaser, I. (1993). The aurora at quiet magnetospheric conditions: Repeatability and dipole tilt angle dependence. *Journal of Geophysical Research*, *98*(A3), 3789–3797. <https://doi.org/10.1029/92JA01950>
- Redmon, R. J., Peterson, W. K., Andersson, L., Kihn, E. A., Denig, W. F., Hairston, M., & Coley, R. (2010). Vertical thermal O⁺ flows at 850 km in dynamic auroral boundary coordinates. *Journal of Geophysical Research*, *115*(A11), 0–08. <https://doi.org/10.1029/2010JA015589>
- Rostoker, G., Akasofu, S.-I., Foster, J., Greenwald, R., Kamide, Y., Kawasaki, K., et al. (1980). Magnetospheric substorms—Definition and signatures. *Journal of Geophysical Research*, *85*(A4), 1663–1668. <https://doi.org/10.1029/JA085IA04P01663>
- Rostoker, G., Friedrich, E., & Dobbs, M. (1996). Physics of magnetic storms. *Geophysical Monograph Series*, *98*, 149–160. <https://doi.org/10.1029/GM098P0149>
- Vanhamäki, H., & Juusola, L. (2020). Introduction to spherical elementary current systems. In *Ionospheric multi-spacecraft analysis tools* (pp. 5–33). Springer International Publishing. https://doi.org/10.1007/978-3-030-26732-2_12
- Viljanen, A., Juusola, L., Kellinsalmi, M., Käki, S., Nielsen, K., Olsen, N., & Xiong, C. (2020). Data, innovation, and science cluster validation of auroral electrojet and auroral boundaries estimated from Swarm observations. Technical Report. <https://earth.esa.int/eogateway/documents/20142/37627/Validation-auroral-electrojet-auroral-boundaries-estimated-from-swarm.pdf>
- VirES for Swarm [Dataset]. (2023). Retrieved from <https://vires.services/>
- Virtanen, P., Gommers, R., Oliphant, T. E., Haberland, M., Reddy, T., Cournapeau, D., et al. (2020). SciPy 1.0: Fundamental algorithms for scientific computing in Python. *Nature Methods*, *17*(3), 261–272. <https://doi.org/10.1038/s41592-019-0686-2>
- Walker, S., Laundal, K., Reistad, J., Ohma, A., & Hatch, S. (2023). Statistical temporal variations in the auroral electrojet estimated with ground magnetometers in Fennoscandia. *Space Weather*, *21*(1), e2022SW003305. <https://doi.org/10.1029/2022SW003305>
- Walker, S. J., Laundal, K. M., Reistad, J. P., Hatch, S. M., & Ohma, A. (2022). Statistics of temporal variations in the auroral electrojets over Fennoscandia- Dataset [Dataset]. <https://doi.org/10.5281/zenodo.6505230>
- Walker, S. J., Laundal, K. M., Reistad, J. P., Hatch, S. M., Ohma, A., Chisham, G., & Decotte, M. (2023). A comparison of auroral oval proxies with the boundaries of the auroral electrojets [Dataset]. <https://doi.org/10.5281/ZENODO.8318792>
- Xiong, C., & Lühr, H. (2014). An empirical model of the auroral oval derived from CHAMP field-aligned current signatures – Part 2. *Annales Geophysicae*, *32*(6), 623–631. <https://doi.org/10.5194/angeo-32-623-2014>
- Xiong, C., Lühr, H., Wang, H., & Johnsen, M. G. (2014). Determining the boundaries of the auroral oval from CHAMP field-aligned current signatures - Part 1. *Annales Geophysicae*, *32*(6), 609–622. <https://doi.org/10.5194/angeo-32-609-2014>
- Zou, Y., Nishimura, Y., Lyons, L. R., & Donovan, E. F. (2012). A statistical study of the relative locations of electron and proton auroral boundaries inferred from meridian scanning photometer observations. *Journal of Geophysical Research*, *117*(A6), 6206. <https://doi.org/10.1029/2011JA017357>